

See discussions, stats, and author profiles for this publication at: <https://www.researchgate.net/publication/236343609>

Structure and Microstructure of Epitaxial $\text{Sr}_4\text{Fe}_6\text{O}_{13+\delta}$ Films on SrTiO_3

ARTICLE in CHEMISTRY OF MATERIALS · JUNE 2004

Impact Factor: 8.35 · DOI: 10.1021/cm0498234

CITATIONS

26

READS

21

5 AUTHORS, INCLUDING:



Marta D Rossell

Empa - Swiss Federal Laboratories for Materi...

111 PUBLICATIONS 3,782 CITATIONS

SEE PROFILE



Jose A. Pardo

University of Zaragoza

43 PUBLICATIONS 512 CITATIONS

SEE PROFILE

Structure and Microstructure of Epitaxial $\text{Sr}_4\text{Fe}_6\text{O}_{13\pm\delta}$ Films on SrTiO_3

Marta D. Rossell,[†] Artem M. Abakumov,^{†,‡} Gustaaf Van Tendeloo,^{*,†}
José A. Pardo,[§] and José Santiso[§]

EMAT, University of Antwerp, Groenenborgerlaan 171, B-2020, Antwerp, Belgium,
Department of Chemistry, Moscow State University, Moscow 119992, Russia, and Instituto de
Ciencia de Materiales de Barcelona, CSIC, Campus UAB, E-08193 Bellaterra, Spain

Received February 3, 2004. Revised Manuscript Received March 29, 2004

The crystal structure and the microstructure of epitaxial $\text{Sr}_4\text{Fe}_6\text{O}_{13\pm\delta}$ thin films grown on a single-crystal SrTiO_3 substrate by PLD have been investigated. A combination of electron diffraction and high-resolution microscopy allows us to refine the structure and to identify an incommensurate modulation in the $\text{Sr}_4\text{Fe}_6\text{O}_{13\pm\delta}$ films. The incommensurate structure ($q = \alpha a_m^* \approx 0.39 a_m^*$, superspace group $Xmmm(\alpha 00)0s0$) can be interpreted as an oxygen-deficient modification in the $\text{Fe}_2\text{O}_{2.5}$ double layers. Moreover, it is shown that the experimentally determined α component of the modulation can be used consistently to estimate the local oxygen content in the $\text{Sr}_4\text{Fe}_6\text{O}_{13\pm\delta}$ films. The compound composition can therefore be described as $\text{Sr}_4\text{Fe}_6\text{O}_{12+2\alpha}$ and the value $\alpha = 0.39$ corresponds to a $\text{Sr}_4\text{Fe}_6\text{O}_{12.78}$ composition. The misfit stress along the $\text{Sr}_4\text{Fe}_6\text{O}_{13\pm\delta}/\text{SrTiO}_3$ interface is accommodated via both elastic deformation and inelastic mechanisms (misfit dislocations and 90° rotation twins). The present results also suggest the existence of SrFeO_3 perovskite in the $\text{Sr}_4\text{Fe}_6\text{O}_{13\pm\delta}$ films.

1. Introduction

Mixed conducting oxides with high oxygen and electronic conductivity have attracted special attention because they hold great promise for industrial use as oxygen separation membranes for selective oxidation of hydrocarbons and electrodes in solid oxide fuel cells. These processes require intermediate and high operating temperatures and substantially different oxygen partial pressures. Therefore, stability of the ceramic membranes is an important issue. However, perovskite oxides containing transition metals with variable oxidation states can change the stoichiometry and consequently induce structural transformations and instabilities at elevated temperatures.^{1–3}

Perovskite-related oxides based on the late 3d transition metals are extensively studied as membrane materials. In this group, the layered perovskite-like phases based on $\text{Sr}_4\text{Fe}_6\text{O}_{13\pm\delta}$ are receiving significant attention.^{4–13}

Several groups have reported data on materials with nominal composition $\text{Sr}_4\text{Fe}_{6-x}\text{Co}_x\text{O}_{13\pm\delta}$.^{7–11} Cobalt-substituted $\text{Sr}_4\text{Fe}_6\text{O}_{13\pm\delta}$ presents high values of oxygen and electronic conductivity with appreciable oxygen permeability at elevated temperatures.^{7–10} Nevertheless, stability of the $\text{Sr}_4\text{Fe}_{6-x}\text{Co}_x\text{O}_{13\pm\delta}$ phase has been questioned. It was found that the cobalt solubility in $\text{Sr}_4\text{Fe}_{6-x}\text{Co}_x\text{O}_{13\pm\delta}$ is very limited and with increasing sintering temperature and increasing Co content it is no longer a single phase, but presents variable amounts of $\text{SrFe}_{1-x}\text{Co}_x\text{O}_{3-\delta}$ perovskite together with an Fe–Co-oxide phase (usually spinel).^{8–11}

Although a lot of research has been dedicated to bulk $\text{Sr}_4\text{Fe}_6\text{O}_{13\pm\delta}$, little attention has been focused on $\text{Sr}_4\text{Fe}_6\text{O}_{13\pm\delta}$ thin films. Recently, high-quality $\text{Sr}_4\text{Fe}_6\text{O}_{13\pm\delta}$ epitaxial thin films on SrTiO_3 were obtained by pulsed laser deposition (PLD).¹²

It is a well-known fact that in a stressed thin film the local structure, and even the symmetry, may differ from that in the bulk. Strain due to lattice mismatch may induce lattice distortions and atom displacements. This is important because crystal orientation, defects, and interface structure will considerably determine the properties of the film. Therefore, a detailed character-

* To whom correspondence should be addressed. Tel: +32 3 265 3262. Fax: +32 3 265 3257. E-mail: gvt@ruca.ua.ac.be.

[†] EMAT, University of Antwerp.

[‡] Moscow State University.

[§] Instituto de Ciencia de Materiales de Barcelona, CSIC.

(1) Kruidhof, H.; Bouwmeester, H. J. M.; Vondoor, R. H. E.; Burggraaf, A. J. *Solid State Ionics* **1993**, 63–65, 816.

(2) Qiu, L.; Lee, T. H.; Liu, L. M.; Yang, Y. L.; Jacobson, A. J. *Solid State Ionics* **1995**, 76, 321.

(3) Kim, S.; Yang, Y. L.; Christoffersen, R.; Jacobson, A. J. *Solid State Ionics* **1997**, 104, 57.

(4) Manthiram, A.; Prado, F.; Armstrong, T. *Solid State Ionics* **2002**, 152, 647.

(5) Avdeev, M. Y.; Patrakeeve, M. V.; Kharton, V. V.; Frade, J. R. J. *Solid State Electrochem.* **2002**, 6, 217.

(6) Patrakeeve, M. V.; Mitberg, E. B.; Leonidov, I. A.; Kozhevnikov, V. L. *Solid State Ionics* **2001**, 139, 325.

(7) Ma, B.; Balachandran, U. *Solid State Ionics* **1997**, 100, 53.

(8) Ma, B.; Hodges, J. P.; Jorgensen, J. D.; Miller, D. J.; Richardson, J. W.; Balachandran, U. *J. Solid State Chem.* **1998**, 141, 576.

(9) Guggilla, S.; Manthiram, A. *J. Electrochem. Soc.* **1997**, 144, L120.

(10) Fjellvåg, H.; Hauback, B. C.; Bredesen, R. *J. Mater. Chem.* **1997**, 7, 2415.

(11) Fossdal, A.; Sagdahl, L. T.; Einarsrud, M. A.; Wiik, K.; Grande, T.; Larsen, P. H.; Poulsen, F. W. *Solid State Ionics* **2001**, 143, 367.

(12) Pardo, J. A.; Santiso, J.; Solís, C.; García, G.; Figueras, A.; Rossell, M. D.; Van Tendeloo, G. *J. Cryst. Growth* **2004**, 262, 334.

(13) Yoshiasa, A.; Ueno, K.; Kanamaru, F.; Horiuchi, H. *Mater. Res. Bull.* **1986**, 21, 175.

ization of $\text{Sr}_4\text{Fe}_6\text{O}_{13\pm\delta}$ thin films becomes essential to understanding, and thereafter manipulating, the conductive properties of epitaxial $\text{Sr}_4\text{Fe}_6\text{O}_{13\pm\delta}$ thin films.

In the present paper, we consider epitaxial $\text{Sr}_4\text{Fe}_6\text{O}_{13\pm\delta}$ thin films deposited on a (001) oriented SrTiO_3 substrate. High-resolution transmission microscopy (HRTEM) and electron diffraction (ED) enable us to determine the structure and the microstructure of the films.

2. Experimental Section

Epitaxial $\text{Sr}_4\text{Fe}_6\text{O}_{13\pm\delta}$ (SFO) thin films were grown on polished (001) oriented SrTiO_3 (STO) substrates by PLD using a Nd:YAG laser with tripled frequency (355 nm wavelength), 9 ns pulse length, 10 Hz repetition rate, and $2\text{--}3\text{ J/cm}^2$ energy density per pulse. The targets for the ablation experiment were prepared by solid-state reaction from a stoichiometric mixture of SrCO_3 and Fe_2O_3 . The resultant powder was milled, uniaxially pressed into pellets, and finally sintered in air at 1150°C . X-ray diffraction measurements confirmed that the target was the single phase $\text{Sr}_4\text{Fe}_6\text{O}_{13\pm\delta}$, as determined by Yoshiasa et al.¹³ During deposition, the substrate temperature was kept at 750°C and the oxygen pressure in the chamber was settled at 3×10^{-2} mbar. After the samples were deposited, they were cooled at 10°C/min under the same atmosphere. Details of the X-ray diffraction studies and scanning electron microscopy are found in Pardo et al.¹²

Samples for TEM were prepared in cross-section and in plan-view. Cross-section samples were cut parallel to the (100) and (110) planes of the STO substrate and mechanically ground to a thickness of about $20\text{ }\mu\text{m}$, followed by final ion-milling under grazing incidence until electron transparency. Plan-view specimens were prepared parallel to the (001) plane of the substrate by thinning from the substrate side. Electron diffraction (ED) and high-resolution electron microscopy (HREM) studies were performed using a JEOL 4000EX microscope. Energy-dispersive X-ray (EDX) analysis was carried out with a Philips CM20 microscope equipped with a LINK-2000 attachment. For the EDX analysis, results were based on the Fe (K) and Sr (K) lines in the spectra. Image simulations were made using the MacTempas software. The NIH Image 1.60 software was used for image processing.

3. Structural Considerations

The crystal structure of $\text{Sr}_4\text{Fe}_6\text{O}_{13\pm\delta}$ (SFO), prepared for the first time by Kanamaru et al.,¹⁴ is orthorhombic and can be described using the acentric *Iba2* space group; the absence of a mirror plane perpendicular to the *c* axis is the result of slight shifts of the Fe atoms located in the $z = 0$ plane.¹³ The lattice parameters are $a = 1.1103(4)\text{ nm}$, $b = 1.8924(4)\text{ nm}$, and $c = 0.5572(2)\text{ nm}$. The structure is built up of SrO and FeO_2 perovskite-type layers alternating along the *b*-direction with $\text{Fe}_2\text{O}_{2.5}$ layers of five-coordinated iron polyhedra (Figure 1). Three nonequivalent sites of iron atoms were found, one octahedral and two five-coordinated positions: trigonal bipyramidal and square pyramidal.¹³ Oxide-ion conduction was assumed to be strictly two-dimensional, confined to the layers formed by the pyramids and bipyramids. On the other hand, the perovskite-like layers supply the primary conducting paths for the electron charge carriers.^{7,9} The $\text{Sr}_4\text{Fe}_6\text{O}_{13\pm\delta}$ unit cell (*a*, *b*, *c*) is closely related to perovskite with a lattice-relation given by $a \approx 2\sqrt{2} \cdot a_p$, $b \approx 5 \cdot a_p$, $c \approx \sqrt{2} \cdot a_p$, where a_p is the basic perovskite cell.

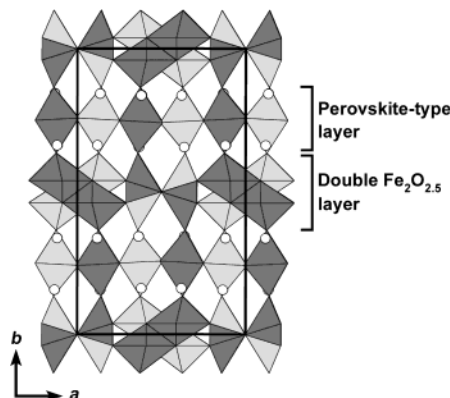


Figure 1. Schematic representation of the $\text{Sr}_4\text{Fe}_6\text{O}_{13\pm\delta}$ crystal structure along the *c*-direction, showing the perovskite-type layers and the double $\text{Fe}_2\text{O}_{2.5}$ layers. The different shades are intended to emphasize that the perovskite slabs are geometrically shifted by $(1/4)a$ or $(1/2)c$ with respect to each other. The circles indicate the Sr positions.

The room-temperature structure of the SrTiO_3 (STO) substrate is well established; it is a cubic perovskite with space group $Pm\bar{3}m$ and lattice parameter $a_{\text{STO}} = 0.3905\text{ nm}$.¹⁵

The misfit along the interface is defined as $\delta = 2 \cdot |a_1 - a_2| / (a_1 + a_2)$ (where a_1 and a_2 are lattice parameters). In our particular case, $\delta_{\text{STO/SFO}(a)} = 0.52\%$ and $\delta_{\text{STO/SFO}(c)} = 0.89\%$. The lattice mismatch between substrate and deposited film is small, but causes the epitaxial film to be strained: the set of pseudocubic planes of the film material is under a small compressive stress. The out-of-plane *b* parameter should therefore elongate to compensate for the cell volume changes.

4. Results

4.1. Reciprocal Space. ED patterns of the SFO/STO sample along $[102]^*_{\text{SFO}}$, $[001]^*_{\text{SFO}}$, and $[010]^*_{\text{SFO}}$ are shown in Figure 2a, b, and c, respectively. The EDs are a superposition of the patterns from substrate and film. The more intense reflections are due to the substrate, whereas the weaker ones are due to the film.

The $[102]^*$ pattern shows an intensity and spot distribution typical for the bulk SFO compound. However, small variations in cell parameter are observed in the strained SFO film. Compared with bulk material, the SFO films show an elongated *b* parameter $\approx 1.9\text{ nm}$, which is in good agreement with the X-ray diffraction study of Pardo et al.¹² The more intense STO reflections form a square pattern. The following epitaxial relation is found: $[001]_{\text{STO}} \parallel [010]_{\text{SFO}}$, $(010)_{\text{STO}} \parallel (201)_{\text{SFO}}$. SFO films grow with the *b*-axis perpendicular to the interface, with *a*- and *c*-axes being oriented along the $\langle 110 \rangle_{\text{STO}}$ directions.

The $[001]^*_{\text{SFO}}$ and $[010]^*_{\text{SFO}}$ patterns in Figure 2b and 2c show clear differences with bulk SFO. The reflections of these patterns can be divided into two sets. The brighter spots can be indexed on an orthorhombic lattice with cell parameters $a_m = 1/2a$, $b_m = b$, and $c_m = c$, where *a*, *b*, and *c* are the lattice parameters of $\text{Sr}_4\text{Fe}_6\text{O}_{13\pm\delta}$. Besides these main reflections, weaker satellite reflections present on both patterns suggest the formation

(14) Kanamaru, F.; Shimada, M.; Koizumi, M. *J. Phys. Chem. Solids* **1972**, *33*, 1169.

(15) Brous, J.; Fankuchen, I.; Banks, E. *Acta Crystallogr.* **1953**, *6*, 67.

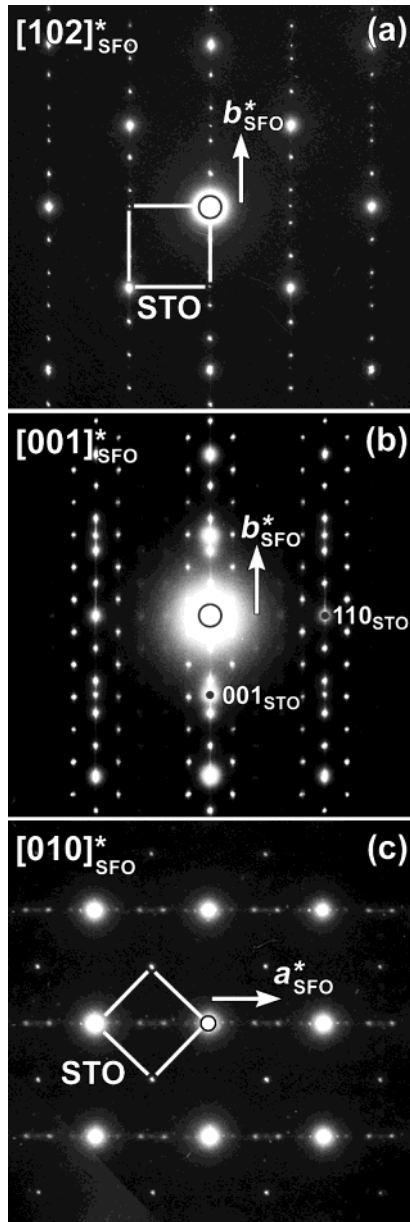


Figure 2. ED patterns of the SFO/STO specimen along (a) $[102]^*_{\text{SFO}}$, (b) $[001]^*_{\text{SFO}}$, and (c) $[010]^*_{\text{SFO}}$. The EDs are a superposition of the patterns from substrate and film.

of a modulated structure. The $[102]^*_{\text{SFO}}$, $[001]^*_{\text{SFO}}$, and $[010]^*_{\text{SFO}}$ patterns can be completely indexed assuming a modulated structure with modulation vector $\mathbf{q} = \alpha a_m^* \approx 0.39 a_m^*$. The indexation scheme for the $[001]^*_{\text{SFO}}$ and $[010]^*_{\text{SFO}}$ pattern is shown in Figure 3c and d. It is important to realize that the reciprocal lattice of bulk $\text{Sr}_4\text{Fe}_6\text{O}_{13\pm\delta}$ can be interpreted as a commensurate modulated structure with $\mathbf{q} = \alpha a_m^* = \frac{1}{2} a_m^*$, as shown in Figure 3a and b. The SFO thin film structure can therefore be described as a superstructure with an α component of the modulation vector, different from that of the bulk material. The proposed choice of the main lattice and the \mathbf{q} vector assumes the presence of reflection conditions which can be derived from the diffraction patterns as $HKLm$: $H + K + m = 2n$, $H + L = 2n$, $K + L + m = 2n$; $H0Ln$: $m = 2n$. The (3+1)D superspace group $Xmmm(\alpha 00)0s0$ corresponds to these conditions, where X stands for the conventional basis with the centering vectors $(0, \frac{1}{2}, \frac{1}{2}, \frac{1}{2})$, $(\frac{1}{2}, 0, \frac{1}{2}, 0)$, $(\frac{1}{2}, \frac{1}{2}, 0, \frac{1}{2})$. On

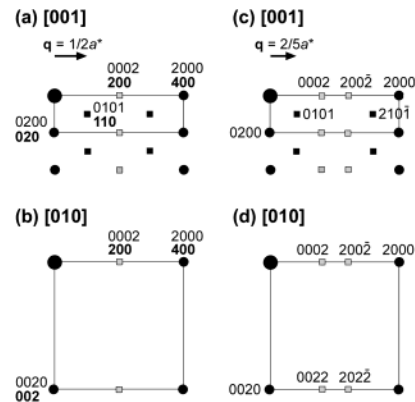


Figure 3. Indexation scheme of the $[001]$ and $[010]$ ED patterns for the $\text{Sr}_4\text{Fe}_6\text{O}_{13\pm\delta}$ (a) and (b), and the SFO film (c) and (d). Main reflections, and first-order and second-order satellites are marked as circles, and black and gray squares, respectively.

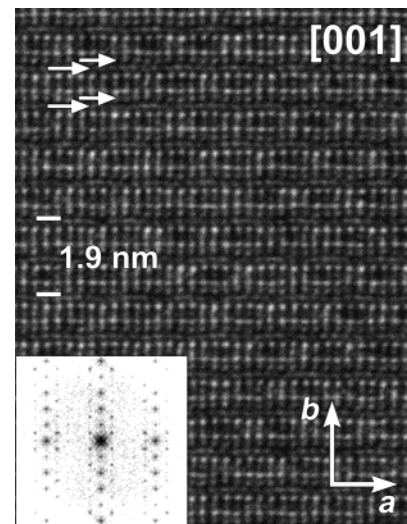


Figure 4. Cross-section HREM image of the SFO film along the c -direction, showing the incommensurate modulation. The SrO layers, imaged as dark dots with a waving intensity, are indicated by arrows. The corresponding FT pattern is shown as an inset.

a primitive basis this corresponds to the superspace group $Fmmm(\alpha 10)0s0$.

The presence in the ED patterns of diffuse streaks along the b^* axis (Figure 2) is related to the presence of planar (010) defects. This will be clear when considering the real space imaging.

4.2. Real Space. **4.2.1. Cross-Section Imaging.** Cross-section TEM shows that the SFO film is uniform with an average thickness of 60 nm. The image reveals a sharp and well-defined interface.

A $[001]$ HREM image and the corresponding Fourier transform (FT) are shown in Figure 4. The visible repeat period along the b -axis corresponds to the SFO alternating sequence of layers. A comparison of the observed and simulated images, based on the bulk SFO structure, shows some clear differences, but under the imaging conditions of Figure 4, dark dots represent columns of heavy atoms. The SrO layers (indicated by arrows) are imaged as dark dots with a waving intensity. The FT pattern of the HREM image (inset Figure 4) exhibits a spot distribution similar to that of the corresponding ED pattern in Figure 2b.

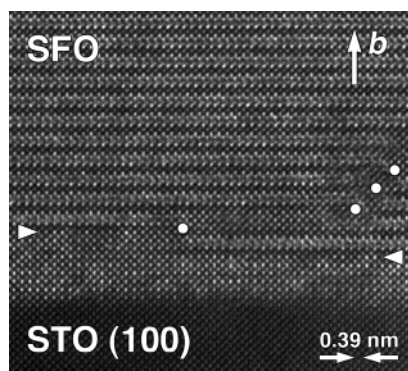


Figure 5. Cross-section HREM image of the SFO/STO(001) interface (indicated by arrowheads). The presence of a buffer layer of more intense contrast below the arrowheads originates the creation of an antiphase boundary (indicated by dots). The b -axis of SFO is also indicated.

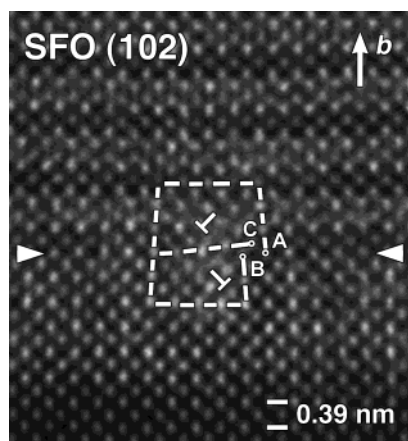


Figure 6. HREM image of a misfit dislocation at the SFO/ SrFeO_3 interface composed of two partials, as denoted by the Burgers circuits.

At the film–substrate interface a buffer layer is formed. It has a perovskite structure and exhibits a variable thickness ranging from 2 to 10 perovskite unit cells. The image contrast is similar to that of the STO substrate, but with a clear difference in intensity (Figure 5). Considering the STO substrate has a perovskite structure and $\text{Sr}_4\text{Fe}_6\text{O}_{13\pm\delta}$ is perovskite-related, it is safe to conceive that the perovskite stacking will remain continuous across the interface. A nanosize slab of SrFeO_3 perovskite-type buffer layer is therefore formed between the substrate and the film. The appearance of this layer with variable thickness is also at the origin of the antiphase boundaries (APB) frequently observed in the film (Figure 5, right part).

APBs usually start at the interface and grow under an angle of 45 degrees with respect to the interface. Occasionally, however, the APBs start and/or end at stacking faults. These stacking faults insert an extra FeO_2 plane in the structure and cause the $\text{Fe}_2\text{O}_{2.5}$ layers to be laterally interrupted and connected with the perovskite-type layers. Most APBs have a displacement vector $\mathbf{R} \approx \frac{1}{5}[\mathbf{101}]_b$. Dislocations are often detected at the interface between the SrFeO_3 buffer layer and the SFO film and contribute to the relief of the misfit stress. Figure 6 shows a HREM image of such a dislocation surrounded by a Burgers circuit with a projected Burgers vector $b[010]$ (AB). Bright dots represent columns of heavy atoms. The length of the projected Burgers



Figure 7. Cross-section HREM image of the interface between the SFO film and the SrFeO_3 buffer layer. A calculated image based on a model where the interface common layer is an octahedral layer, for a defocus value $\Delta f = -70$ nm and a thickness $t = 4$ nm, is shown as an inset. The arrowheads indicate the position of the SFO/ SrFeO_3 interface.

vector is a_p ($a_p \approx 0.39$ nm). However, a close inspection shows that the dislocation is dissociated and composed of two partial dislocations located in the (010) SrFeO_3 plane, perpendicular to the projected total Burgers vector. This can be clearly seen from the two sub-circuits CA and CB in Figure 6. The two partials have a projected Burgers vector of $[0, \frac{b}{2}, \frac{c}{2}]$ and $[0, \frac{b}{2}, -\frac{c}{2}]$ respectively. The two partials have the same b -axis but an opposite c -component.

The image simulation of the SFO/ SrFeO_3 interface (inset in Figure 7) confirms that under the experimental defocus conditions the bright dots correspond to the heavy atom columns. The excellent fit with the experimental image of the SFO/ SrFeO_3 interface supports the idea that the common layer between the SrFeO_3 buffer and the SFO film is the octahedral layer. In the simulation no oxygen deviation has been taken into account, but this would hardly alter the intensities.

Occasionally these SrFeO_3 perovskite slabs also appear as intergrowth within the film; they have a pancake shape with nanometer width, but with 100-nm lateral dimensions. These SrFeO_3 perovskite slabs mostly appear in the upper half of the film and grow through the complete film.

4.2.2. Plan View. Plan-view images along the b_{SFO} -axis show that the SFO films are flat, but with elongated precipitates oriented along two mutually perpendicular directions parallel to $[100]_{\text{SFO}}$ and $[001]_{\text{SFO}}$ (Figure 8a). The corresponding ED pattern is shown in Figure 8b; this pattern is a superposition of the patterns from substrate, film, and precipitates. The most intense reflections, which exhibit a square pattern, are due to the substrate, the film, and the precipitates, whereas the weaker spots are exclusively due to the SFO film and the precipitates. The ED pattern is typical of a twinned structure resulting from domains that have mutually perpendicular a and c -axes. Figure 8a is indeed a dark-field image taken with the objective aperture positioned around the reflection outlined by a white circle in Figure 8b. These reflections are clearly associated with the precipitates, which show up bright in Figure 8a.

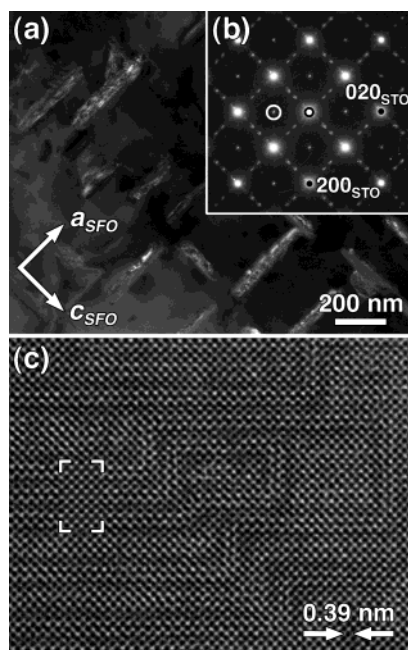


Figure 8. (a) Dark-field image of the SFO thin film along the b -axis, showing the presence of elongated precipitates with two mutually perpendicular directions. (b) Corresponding ED pattern. The dark-field image in (a) was taken with an objective aperture positioned in the reflection outlined by a white circle. (c) Plan-view HREM image showing the presence of labyrinth-shape planar defects in the SrFeO_3 perovskite precipitates. A calculated image of the planar defects based on the insertion of an extra salt-type layer, for a defocus value $\Delta f = -77$ nm and a thickness $t = 3.5$ nm, is shown as an inset.

The iron and strontium content of the film and the precipitates was evaluated by EDX analysis performed inside the electron microscope. To estimate the quantification error for each element, twenty spectra were recorded. The SFO film contains (40.2 ± 1.4) % Sr and (59.8 ± 1.4) % Fe, while the precipitates contain roughly a similar amount of iron and strontium.

The HREM contrast of such a precipitate is typical for a perovskite-type structure with planar defects along two perpendicular directions creating a labyrinth-type pattern (Figure 8c). Combined data from HREM, ED, and EDX point toward a perovskite-type structure with composition SrFeO_3 for the elongated precipitates. The labyrinth-shaped planar defects are due to the insertion of an extra SrO rock salt-type layer in the SrFeO_3 structure resulting in a shift over $a_p/2$ between adjacent layers along a direction parallel to the SrO layer. The image simulation (inset Figure 8c) based on the proposed model shows a good fit with the experimental image.

5. Discussion

5.1. SFO Crystal Structure. The major problem concerns the crystal structure of the SFO film. The SFO in the film and the bulk $\text{Sr}_4\text{Fe}_6\text{O}_{13\pm\delta}$ phase clearly have the same sublattice but differ by the position of the satellite reflections. The EDX analysis of the pure SFO film (no precipitates) reveals a Sr/Fe ratio of 4:6, indicating that no significant changes are introduced into the cation sublattice of the SFO film in comparison with the bulk material. One may therefore assume that the changes in the crystal structure are caused by a

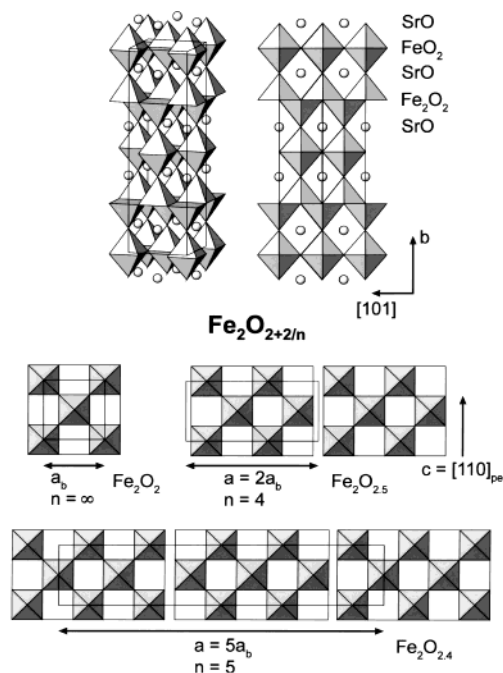


Figure 9. Top: 3D view and $[101]$ projection of the idealized $\text{Sr}_4\text{Fe}_6\text{O}_{12}$ structure. Bottom: schematic representation of the Fe_2O_2 , $\text{Fe}_2\text{O}_{2.5}$, and $\text{Fe}_2\text{O}_{2.4}$ layers. The FeO_5 square pyramids point up and below the layer plane.

difference in oxygen content. HREM and ED allow proposal of a possible relationship between the oxygen content in the $\text{Sr}_4\text{Fe}_6\text{O}_{13\pm\delta}$ phases, the α component of the modulation vector \mathbf{q} , and the structural changes induced by a changing oxygen stoichiometry.

An idealized parent structure model for the $\text{Sr}_4\text{Fe}_6\text{O}_{13\pm\delta}$ phases can be built with the $Fm\bar{3}m$ space group in a unit cell with $a = \sqrt{2} \cdot a_p$, $b = 4 \cdot a_p$, $c = \sqrt{2} \cdot a_p$ (a_p = the parameter of perovskite subcell) (Figure 9, top). This unit cell and space group are responsible for the sublattice of the main reflections of the bulk $\text{Sr}_4\text{Fe}_6\text{O}_{13\pm\delta}$ and the SFO film. The structure is built up of SrO , FeO_2 , and Fe_2O_2 layers, where the SrO and FeO_2 layers are identical to the AO and BO₂ layers of the ideal ABO₃ perovskite structure. The Fe_2O_2 layer represents a fragment of an NaCl structure and consists of edge-sharing oxygen squares filled with Fe. The layers alternate along the b axis according to the sequence $-\text{SrO}-\text{FeO}_2-\text{SrO}-\text{Fe}_2\text{O}_2-\text{SrO}-$ (Figure 9, top). The coordination environment of Fe in the Fe_2O_2 layers is completed to a square pyramid by the oxygen atoms from the two neighboring SrO layers. Thus, a chess-board pattern of square pyramids with apical vertexes directed up and down is formed (Figure 9, bottom). This idealized structure has a composition $\text{Sr}_4\text{Fe}_6\text{O}_{12}$. Because the perovskite-type layer does not acquire extra oxygen or anion vacancies when δ is varied in $\text{Sr}_4\text{Fe}_6\text{O}_{13\pm\delta}$,^{5,16} an oxygen nonstoichiometry can only be induced by a variable composition in the NaCl-type layer. Additional oxygen atoms can be inserted into these Fe_2O_2 layers as extra rows of anions running along the $c = [110]_p$ direction. Extra oxygen rows break the infinite Fe_2O_2 into bands of edge-sharing FeO_5 pyramids with a limited extension along the a axis. If the extra

(16) Waerenborgh, J. C.; Avdeev, M.; Patrakeev, M. V.; Kharton, V. V.; Frade, J. R. *Mater. Lett.* **2003**, *57*, 3245.

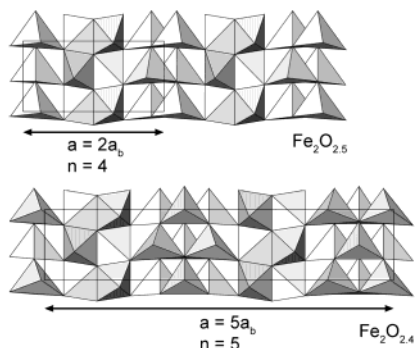


Figure 10. FeO_5 polyhedra arrangement in the $\text{Fe}_2\text{O}_{2.5}$ layer (top) and the $\text{Fe}_2\text{O}_{2.4}$ layer (bottom).

oxygen rows create bands with a width of n FeO_5 pyramids, the composition of the layer can be written as $\text{Fe}_2\text{O}_{2+2/n}$ resulting in a $\text{Sr}_4\text{Fe}_6\text{O}_{12+4/n}$ phase composition. Two examples where bands with $n = 4$ and $n = 5$ are formed are shown in Figure 9. The former corresponds to the SFO bulk phase, whereas the latter, as will be shown below, provides a good approximation for the structure of the SFO film.

The extra oxygen rows alternate in an ordered manner along the a axis resulting in the appearance of satellite reflections along a^* . The thickness n of the bands is then directly related to the α component of the modulation vector \mathbf{q} as $n = 2/\alpha = x\{n\} + (1-x)(\{n\}+1)$, where $\{n\}$ is the integer part of n , x stands for the fractional part of the bands with a width of n , and $1-x$ is the fractional part of $n+1$ bands. The compound composition can therefore be formulated as $\text{Sr}_4\text{Fe}_6\text{O}_{12+2\alpha}$. The experimental value $\alpha = 0.39$, obtained by ED, therefore corresponds to a composition $\text{Sr}_4\text{Fe}_6\text{O}_{12.78}$ and the structure consists of an alternation of approximately 9 bands of 5 pyramids and 1 band of 6 pyramids.

The proposed building scheme can be formalized in the $(3+1)$ dimensional space using the superspace group and a steplike occupation modulation function for the atoms in the $\text{Fe}_2\text{O}_{2+2/n}$ layers. For simplicity, we restrict ourselves to the commensurate approximation $\alpha = 2/5$; this corresponds to the $\text{Fe}_2\text{O}_{2.4}$ layers shown in Figure 9. Apart from an occupancy modulation, the real structure should also include a significant displacive modulation to avoid extremely short O–O and Fe–O distances. Such displacements were introduced in the idealized model using the obvious analogy with the bulk $\text{Sr}_4\text{Fe}_6\text{O}_{13\pm\delta}$ structure. The comparison between the $\text{Fe}_2\text{O}_{2.5}$ layer in the $\text{Sr}_4\text{Fe}_6\text{O}_{13\pm\delta}$ structure and the $\text{Fe}_2\text{O}_{2.4}$ layer in the $\text{Sr}_4\text{Fe}_6\text{O}_{12.8}$ structure model is given in Figure 10. The displacements result in a transformation of a part of the square pyramids to the trigonal bipyramids and a splitting of the layer along the b axis.

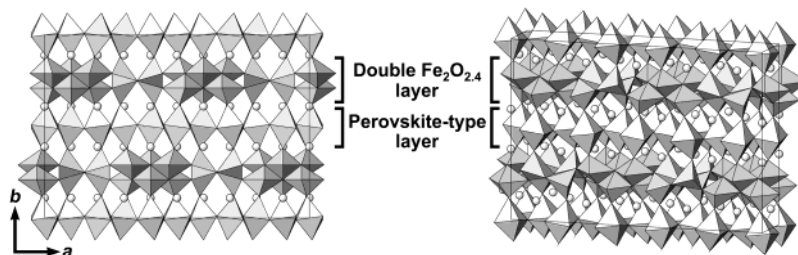


Figure 11. [001] projection and 3D view of the $\text{Sr}_4\text{Fe}_6\text{O}_{12.8}$ structure model, showing the double $\text{Fe}_2\text{O}_{2.4}$ layers and the perovskite-type layers. The white circles represent the Sr ions.

The complete model was built with a space group $Bba2$ and a unit cell with parameters $a = 2.775$ nm, $b = 1.892$ nm, and $c = 0.557$ nm (Figure 11). A calculated image based on this model is shown as an inset in Figure 12, and is in excellent agreement with the experimental image.

The generation of a modulated structure in the SFO films can be related to the oxygen deficiency. This can be quantified; indeed the position of the satellite reflections in the ED patterns allows determination of the oxygen content in the SFO films. Because the $\text{Fe}_2\text{O}_{2+2/n}$ layers formed by pyramids and bipyramids supply the oxygen charge carriers it is assumed that the oxide-ion conduction will be influenced by the deficiency of oxygen content in the SFO films. The oxygen content and the formation of the incommensurate modulation will, of course, also be affected by the misfit stress between the film and the substrate. However, the misfit stress is very low and moreover, the intermediate perovskite layer will partially accommodate the misfit.

It should be noted that a substantial decrease of the oxygen content in $\text{Sr}_4\text{Fe}_6\text{O}_{13\pm\delta}$ requires strongly reducing conditions, such as $T = 1173$ K and $P(\text{O}_2) \approx 10^{-7}$ mbar.⁵ The SFO film was grown at lower temperature (1023 K) and a much higher partial oxygen pressure (3×10^{-2} mbar), so it is hardly possible to expect a reduction of the as-grown material under such conditions. This indicates that the reduced $\text{Sr}_4\text{Fe}_6\text{O}_{13-\delta}$ compounds can not only be obtained by postannealing treatment, but also by direct synthesis at much softer reducing conditions. This conclusion might open a new synthesis route toward reduced $\text{Sr}_4\text{Fe}_6\text{O}_{13-\delta}$ phases with an ordered arrangement of oxygen atoms and anion vacancies in the $\text{Fe}_2\text{O}_{2+2/n}$ layers.

5.2. Microstructure. SFO thin films prepared by PLD on STO apparently contain SrFeO_3 perovskite which is mainly present in two different forms: as a buffer layer between the SFO film and the STO substrate, and as nanosized intergrowths within the film. The SrFeO_3 perovskite and the STO substrate belong to the same space group; they also have a very similar lattice parameter and therefore their reflections superpose in the ED patterns (Figure 2). The epitaxial relation between the SFO film and the SrFeO_3 perovskite is the same as that for the SFO/STO sample: $[001]_{\text{SrFeO}_3} \parallel [010]_{\text{SFO}}$, $(010)_{\text{SrFeO}_3} \parallel (201)_{\text{SFO}}$. The difference in lattice parameter ($a_{\text{SrFeO}_3} < d_{201,\text{SFO}}$) is largely taken up elastically, leading to a somewhat larger a_{SrFeO_3} lattice parameter parallel to the interface.

The STO substrate was chosen to minimize the misfit with the SFO film along the contact plane and to avoid possible mechanical deformation. However, the formation of a SrFeO_3 buffer layer takes place although a_{SrFeO_3}

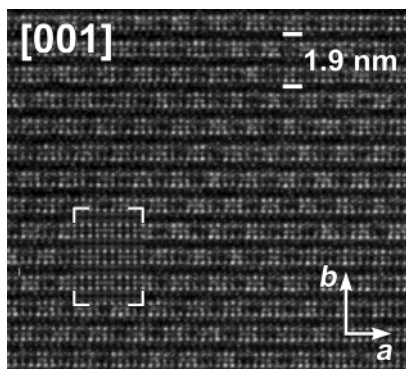


Figure 12. $[001]_{\text{SFO}}$ HREM image showing the incommensurate modulation. A calculated image based on the model of Figure 11, for a defocus value $\Delta f = -85$ nm and a thickness $t = 7$ nm, is shown as an inset.

$< a_{\text{STO}} < d_{201,\text{SFO}}$. The SrFeO_3 buffer layer is sandwiched between two phases with larger lattice parameters. From a purely elastic point of view, it would seem more favorable to form the SFO phase directly on STO because the misfit is smaller ($\delta_{\text{STO}/\text{SFO}(a)} = 0.52\%$ and $\delta_{\text{STO}/\text{SFO}(c)} = 0.89\%$) compared with the SrFeO_3 phase ($\delta_{\text{STO}/\text{SrFeO}_3} = 1.42\%$). Moreover, the misfit between the buffer layer and the SFO film is $\delta_{\text{SrFeO}_3/\text{SFO}(a)} = 1.94\%$ and $\delta_{\text{SrFeO}_3/\text{SFO}(c)} = 2.31\%$. We therefore have to accept that the formation of the perovskite buffer layer not only depends on the lattice mismatch but also on the lattice energy involved at the initial stages of the growth process; the perovskite stacking tends to remain continuous along the interface, leading to the formation of a nanosize SrFeO_3 perovskite-type buffer layer. The variable thickness of this layer promotes the formation of APBs that will certainly influence the oxide-ion conduction, which is assumed to be strictly two-dimensional confined to the double layers. Indeed, the double layers are laterally interrupted and connected with the perovskite-type layers along an APB.

The lattice parameter mismatch between the film and the buffer layer also causes the epitaxial film to be strained. The set of pseudocubic planes of the film material is under a small compressive stress. Thus, the out-of-plane b parameter stretches to compensate for cell volume changes resulting in an elongated b parameter of ~ 1.9 nm. However, the misfit stress cannot be accommodated in the SFO film on STO exclusively via

elastic deformation, and inelastic accommodation mechanisms are required. It is usually assumed that this occurs by the formation of misfit dislocations in the as-grown state. Misfit dislocations are commonly composed of two partials. The misfit stress also promotes the development of 90° rotation twins where the twin domains have mutually perpendicular a and c -axes.

Elongated precipitates of SrFeO_3 , oriented along two mutually perpendicular directions parallel to $[100]_{\text{SFO}}$ and $[001]_{\text{SFO}}$, will also contribute to release the misfit stress. Planar defects observed in plan view (Figure 8c) can be understood, assuming the insertion of an extra SrO rock-salt-type layer in the SrFeO_3 structure; this requires an oxygen deficiency. This requisite is in good agreement with the oxygen-deficient crystal structure proposed for the SFO film.

6. Conclusion

The crystal structure and microstructure of epitaxial $\text{Sr}_4\text{Fe}_6\text{O}_{13\pm\delta}$ thin films grown on a STO single-crystal substrate have been studied. An incommensurate modulation in the thin film can be interpreted as an oxygen-deficient modification. The structure of the modulated phase has been determined from electron diffraction and high-resolution microscopy data. Electron diffraction patterns can consistently be used to estimate the oxygen content in the SFO films.

The misfit stress along the SFO/STO interface is accommodated via both elastic deformation (a_{SFO} and c_{SFO} parameters shorten and the out-of-plane b_{SFO} parameter elongates and compensates for cell volume changes) and inelastic accommodation (misfit dislocations and 90° rotation twins). The present results also suggest the existence of SrFeO_3 perovskite slabs at the SFO/STO interface as well as within the SFO film.

Acknowledgment. This work has been performed within the framework of IAP V-1 of the Belgian government and the GBOU contract of the Flemish government. We acknowledge financial support of the American Chemical Society (PRF 38459-AC5). A.M.A. is grateful to INTAS for the Fellowship grant for Young Scientists YSF 2002-48. Part of this work is supported by the Spanish Science Ministry (project MAT2002-03075) and the CSIC Fuel Cell Network.

CM0498234